

Microwave Hall measurements using a circularly polarized dielectric cavity

M. Roppongi,¹ T. Arakawa,² Y. Yoshino,¹ K. Ishihara,¹ Y. Kinoshita,³ M. Tokunaga,³ Y. Matsuda,⁴ K. Hashimoto,¹ and T. Shibauchi¹

¹*Department of Advanced Materials Science, University of Tokyo, Kashiwa, Chiba 277-8561, Japan*

²*National Institute of Advanced Industrial Science and Technology (AIST), Tsukuba, Ibaraki 305-8563, Japan*

³*Institute for Solid State Physics (ISSP), University of Tokyo, Chiba 277-8581, Japan*

⁴*Department of Physics, Kyoto University, Kyoto 606-8502, Japan*

(*Electronic mail: k.hashimoto@edu.k.u-tokyo.ac.jp)

(*Electronic mail: roppongi@qpm.k.u-tokyo.ac.jp)

(Dated: 16 April 2024)

We have developed a circularly polarized dielectric rutile (TiO₂) cavity with a high quality-factor that can generate circularly polarized microwaves from two orthogonal linearly polarized microwaves with a phase difference of $\pm\pi/2$ using a hybrid coupler. Using this cavity, we have established a new methodology to measure the microwave Hall conductivity of a small single crystal of metals in the skin-depth region. Based on the cavity perturbation technique, we have shown that all components of the surface impedance tensor can be extracted under the application of a magnetic field by comparing the right- and left-handed circularly polarization modes. To verify the validity of the developed method, we performed test measurements on tiny Bi single crystals at low temperatures. As a result, we have successfully obtained the surface impedance tensor components and confirmed that the characteristic field dependence of the ac Hall angle in the microwave region is consistent with the expectation from the dc transport measurements. These results demonstrate a significant improvement in sensitivity compared to previous methods. Thus, our developed technique allows more accurate microwave Hall measurements, opening the way for new approaches to explore novel topological quantum materials, such as time-reversal symmetry-breaking superconductors.

I. INTRODUCTION

The Hall effect, discovered by Edwin Hall in 1879¹, is one of the most fundamental phenomena in solid-state physics, in which electrons in a conductor placed in a magnetic field are subject to the Lorentz force, generating a transverse voltage perpendicular to the current flow in the conductor. The Hall conductivity, which is the off-diagonal component of the conductivity tensor, provides vital information on the type and concentration of charge carriers in a conductor. Hence, Hall measurements have long been performed on a wide variety of materials. Recent observations of the anomalous Hall effect in topological quantum materials with time-reversal symmetry breaking (TRSB) states, in which a Hall voltage is generated even in the absence of a magnetic field, have further highlighted the importance of Hall effect measurements². Therefore, the Hall effect, which is usually investigated in the dc or low-frequency range, is one of the most important probes in solid-state physics.

The Hall effect in the high-frequency region reflects the dynamical conductivity and thus provides more detailed information than the Hall effect in the dc region. Such ac Hall conductivity measurements are usually carried out using the Faraday (Kerr) effect in the THz region³⁻¹³. In these methods, the circular dichroism (CD), which is the response difference between the right and left-handed circularly polarized lights, rotates the polarization axis of the incident linearly polarized light, resulting in a transmitted (reflected) elliptical polarization when σ_{xy} is finite, reflecting TRSB. Since the rotation angle $\theta_{F(K)}$ is proportional to the ac Hall conductivity σ_{xy} , one can obtain information on the dynamical conductivity from the rotation angle. However, such magneto-optical measure-

ments usually require a flat sample surface, and the optical system tends to be complex.

So far, several measurements of the Hall effect in the microwave region have been reported¹⁴⁻³⁷. In such measurements, the Hall component is detected using two orthogonal magnetic field modes in a bimodal cavity. However, most of the previous studies using this technique have been limited to measurements at room temperature on low-conductivity systems such as semiconductors¹⁴⁻³⁴. Recently, Ogawa *et al.*³⁵ have enabled surface impedance tensor measurements in the skin depth region for materials with high conductivity at cryogenic temperatures by using both cross-shaped bimodal and cylindrical cavities. This method is particularly useful for studying phenomena such as the flux flow Hall effect^{36,37}. However, this method requires two different cavities to determine the geometric factor that depends on the sample and cavity geometries.

Recently, Arakawa *et al.* proposed a new method for the measurement of microwave Hall conductivity using a circularly polarized cavity³⁸. In this method, right- and left-handed circularly polarized eigenmodes are created using a cylindrical microwave cavity with a hybrid coupler^{38,39}. The differences in resonance frequency and Q -factor of each circularly polarized mode (i.e., CD) allow the determination of all components of the dynamical conductivity tensor by a non-contact method. The previous study used circularly polarized electric field modes to measure the microwave Hall conductivity of high-resistance materials, such as a two-dimensional electron gas system. In contrast, microwave impedance measurements of highly conductive materials generally require magnetic field modes⁴⁰. However, in the previous study, a copper cavity was used, resulting in a relatively low Q -factor ($Q < 10000$) and low sensitivity, making precise Hall mea-

measurements for conductive materials with small Hall responses difficult.

To extend this technique to more metallic samples, we constructed a circularly polarized cavity with a high Q -factor by using a dielectric rutile. In this paper, we present a new method to precisely measure the microwave Hall effect for tiny conductive samples. We have developed a circularly polarized dielectric rutile TiO_2 cavity with a higher Q -factor than the previous copper cavity even in high magnetic fields^{38,39}. In addition, we have proposed a new protocol to measure all components of the surface impedance tensor in metals from the perturbation response to circularly polarized modes. Furthermore, in this study, we have confirmed the validity of the developed method by performing test measurements on small bismuth (Bi) single crystals. Our method enables more accurate measurements of the microwave Hall effect for conductive materials, which will allow us to explore topological quantum materials with an off-diagonal conductivity component, such as TRSB superconductors.

II. EXPERIMENTAL METHOD

A. Circularly polarized microwave cavity

Circular polarization is the superposition of two orthogonal and degenerate linear polarized waves with a phase difference of $\pm\frac{\pi}{2}$. To realize circularly polarized eigenmodes inside a microwave cavity, an apparatus that can introduce a relative phase difference between two orthogonal and degenerate linearly polarized modes is required. To achieve this, we adopted a cylindrical circularly polarized cavity equipped with a hybrid coupler, as proposed by Arakawa *et al.*^{38,39} Figure 1(a) shows a schematic of the cavity we developed. The main advantage of this system is that the right- and left-handed modes of circular polarization can be easily controlled by switching the input port, which reverses the $\pm\frac{\pi}{2}$ phase difference. In other words, the right- (TM_+) and left- (TM_-)-handed circular polarization modes can be controlled by the vector network analyzer through switching of the scattering parameter (S -parameter) measurements between S_{12} and S_{21} . Furthermore, the hybrid coupler has a compact structure, allowing easy installation in a cryostat.

As mentioned above, the previous circularly polarized cavity was made of copper, resulting in a low Q -factor and low sensitivity. This limits the measurements to samples with a large CD response^{38,39}. Therefore, for measurements on materials exhibiting small Hall responses, improvements in Q -factor and sensitivity are highly required. Superconducting cavities are often used to achieve extremely high Q -factors, but they cannot maintain high Q -factors in magnetic fields^{41,42}. Thus, we have employed a dielectric rutile TiO_2 cavity with a high Q -factor even at low temperatures and in high magnetic fields. Previous studies have reported that the rutile cavity can maintain a high Q factor of $\sim 10^6$ and high-frequency stability (frequency drift < 1 Hz/h) even in high magnetic fields⁴³.

Figure 1(a) shows an overview of the developed circularly polarized rutile cavity. A cylindrical rutile TiO_2 is placed at the center of a cylindrical copper enclosure, on which the input and output ports are equipped through a hybrid coupler.

Figures 1(b) and (c) show the electromagnetic field distributions of the TM mode in the circularly polarized rutile cavity used in this study obtained from the electromagnetic field simulations (software: Ansys Electronics Desktop Student). The magnetic field (H -field) distribution is concentrated at the center of the rutile (Fig. 1(b), right), while the electric field (E -field) is weak (Fig. 1(b), left). As shown in Fig. 1(c), two orthogonal and degenerate linear polarization modes in the xy -plane can generate a circularly polarized mode rotating

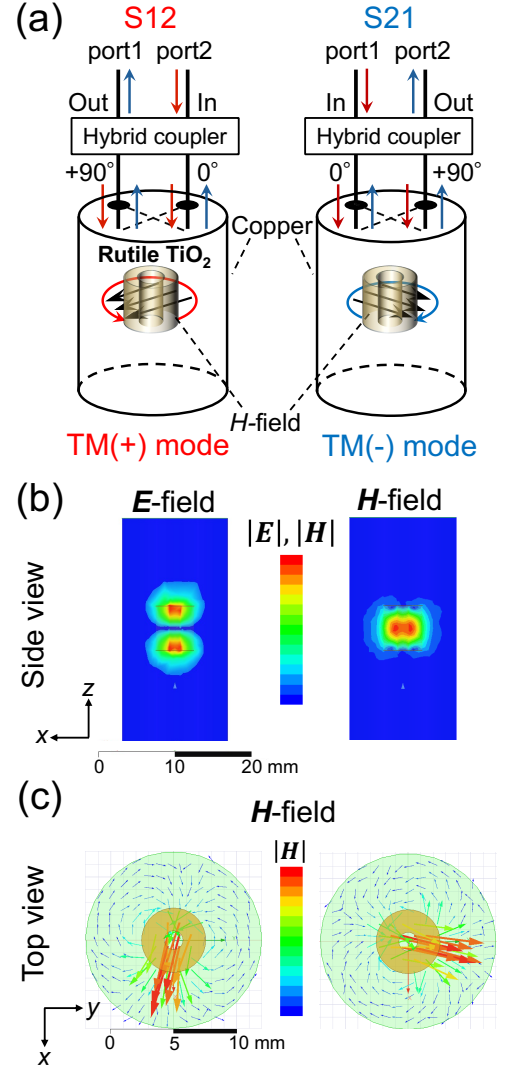


FIG. 1: (a) Schematic of the developed circularly polarized dielectric rutile TiO_2 cavity. The outer and inner diameters of the rutile is $\phi_{out} = 5.1$ mm and $\phi_{in} = 1.5$ mm, respectively, and the height is $L = 5.9$ mm. Here, the cylindrical axis of the rutile cavity corresponds to the c -axis direction, and the plane perpendicular to it corresponds to the ab plane. [(b) and (c)] Simulations of electromagnetic field distribution for the TM mode. The magnitude distributions of the electric and magnetic fields of the TM mode in the vertical cross section at the center of the cavity (b) and the vector distributions of the magnetic fields of the two degenerate TM modes in the horizontal cross section at the center of the cavity (c) are shown.

in the xy -plane at the center of the rutile, which is achieved by introducing a phase difference of $\pm\frac{\pi}{2}$ between the two linear polarization modes through the hybrid coupler. Our electromagnetic field simulations show that the central rutile confines almost all the microwave fields, significantly reducing the shielding currents in the surrounding copper walls, which results in a high Q -factor. Furthermore, using a small rutile cavity, the ratio of the sample volume to the electromagnetic field volume (filling factor) increases, resulting in an increase in sensitivity. In our setup, the resonance frequency obtained from the electromagnetic field simulation is $f_0 \sim 4.24$ GHz at 4 K, while the actual experimental value for the circularly polarized rutile cavity without a sample is $f_0 \sim 4.17$ GHz. The experimentally obtained Q -factor without a sample is $Q_0 \sim 1 \times 10^5$ at 10 K, which is lower than the previously reported $Q_0 \sim 1 \times 10^6$ ⁴³. This is due to the small diameter of the copper enclosure used here, which causes energy loss due to leakage of electromagnetic fields around the copper walls. However, the obtained Q -factor is significantly higher than those in the previous circularly polarized³⁸ and bimodal cavities³⁵, allowing for more sensitive microwave Hall effect measurements in a magnetic field, as shown in the following sections.

B. Surface impedance tensor measurements

Surface impedance is a quantity that represents the resistance per unit area to the ac fields in the skin depth region, and the surface impedance tensor in the xy -plane is expressed as follows³⁵:

$$\hat{Z} = \begin{pmatrix} Z_L & Z_H \\ -Z_H & Z_L \end{pmatrix} = \begin{pmatrix} R_L + iX_L & R_H + iX_H \\ -R_H - iX_H & R_L + iX_L \end{pmatrix}, \quad (1)$$

where $Z_{L(H)}$ is the diagonal (off-diagonal) component of the surface impedance tensor, and $R_{L(H)}$ and $X_{L(H)}$ are the real and imaginary parts of the diagonal (off-diagonal) component, which are the surface (surface Hall) resistance and surface (surface Hall) reactance, respectively.

Most of the surface impedance measurements using the cavity perturbation technique reported so far^{43–47} utilize the H -field of the linearly polarized TE_{011} mode. This method allows the detection of only the diagonal component of the surface impedance, Z_L , from the changes in resonance frequency f and Q -factor. To the best of our knowledge, surface impedance measurements using a circularly polarized H -field mode have not been performed so far. Therefore, in this study, we derive the relationship between the resonance characteristics of circularly polarized H -field modes and the surface impedance tensor in the cavity perturbation technique. As a result, we find the following relationship (the detailed derivation is described in Appendix A):

$$\Delta\left(\frac{1}{2Q_{\pm}}\right) + i\left(\frac{\Delta f_{\pm}}{f_0} + C\right) = G(Z_L \mp iZ_H), \quad (2)$$

where C is the metallic shift, and G is the geometric factor. The indices \pm and 0 represent the right (+) and left (-)-handed polarized modes and the blank without a sample, respectively, and Δ represents the difference before and after sample insertion. From Eq. (2), the components of the surface impedance

tensor can be given by using the resonant frequency f and the

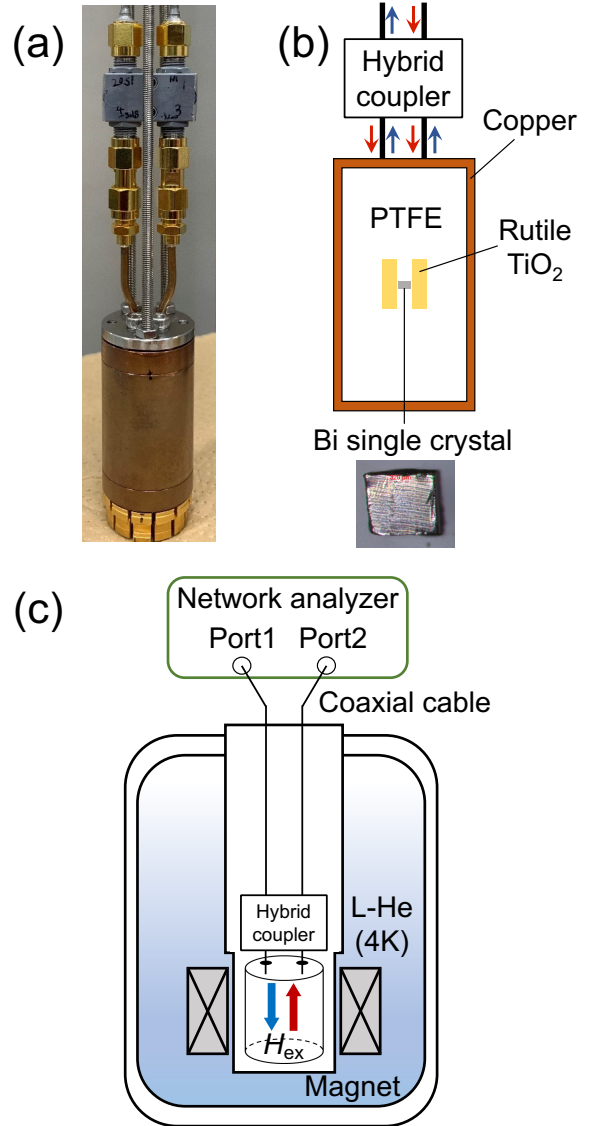


FIG. 2: Experimental setup for the surface impedance tensor measurements using the circularly polarized rutile cavity. (a) Photograph of the cavity fabricated in this study. The top of the cavity is attached to the input and output coaxial cables via a hybrid coupler. A PPMS pack is attached to the bottom of the cavity to achieve good thermal contact with the sample space of the PPMS. (b) Schematic of the circularly polarized rutile cavity. A rutile cavity with a hollowed center is placed inside a copper cavity. In this study, a single-crystal sample of Bi was placed in the center of the rutile cavity. (c) Schematic diagram of the entire measurement system. The temperature and magnetic field are controlled by the PPMS control system. The vector network analyzer (Keysight P5027A) located in the room temperature part measures S_{12} and S_{21} spectra through the semi-rigid coaxial cables.

Q -factor as follows:

$$\frac{1}{2Q_+} - \frac{1}{2Q_0} = G(R_L + X_H), \quad (3a)$$

$$\frac{1}{2Q_-} - \frac{1}{2Q_0} = G(R_L - X_H), \quad (3b)$$

$$\frac{f_+ - f_0}{f_0} = G(X_L - R_H) + C, \quad (3c)$$

$$\frac{f_- - f_0}{f_0} = G(X_L + R_H) + C, \quad (3d)$$

where f_0 and Q_0 are the resonance frequency and Q -factor without a sample, respectively. From Eqs. (3a)-(3d), each component of the surface impedance tensor is expressed as

$$R_L = \frac{1}{4G} \left(\frac{1}{Q_+} + \frac{1}{Q_-} - \frac{2}{Q_0} \right), \quad (4a)$$

$$X_L = \frac{1}{2G} \left(\frac{f_+ + f_- - 2f_0}{f_0} - 2C \right), \quad (4b)$$

$$R_H = -\frac{1}{2G} \left(\frac{f_+ - f_-}{f_0} \right), \quad (4c)$$

$$X_H = \frac{1}{4G} \left(\frac{1}{Q_+} - \frac{1}{Q_-} \right). \quad (4d)$$

Here we emphasize that Eqs. (4c) and (4d) indicate that the difference between the resonance frequencies f_{\pm} and the Q -factors Q_{\pm} in the right and left-handed modes, i.e., CD, is proportional to the off-diagonal term of the surface impedance tensor. Our present method allows in situ measurements of right- and left-handed modes in the same cavity, and G and C are uniquely determined (the detailed analysis procedures are described in the next section). Thus, compared to the previous method³⁵, which requires multiple resonators and several assumptions, this method can more easily and accurately obtain the surface impedance tensor.

Finally, we derive the relationship between the surface impedance tensor and the ac Hall conductivity. The conductivity tensor $\tilde{\sigma}$ and the surface impedance tensor are related by the following expression³⁵:

$$\tilde{Z} = \frac{1}{\delta} \tilde{\sigma}^{-1}, \quad (5)$$

where δ denotes the skin depth. From this relation, Z_L and Z_H are represented by

$$Z_L = \sqrt{\frac{-i\mu_0\omega}{\sigma(\omega)}} \frac{1}{\sqrt{1 \mp i \tan \theta}}, \quad (6a)$$

$$Z_H = \sqrt{\frac{-i\mu_0\omega}{\sigma(\omega)}} \frac{\tan \theta}{\sqrt{1 \mp i \tan \theta}}, \quad (6b)$$

where μ_0 is the vacuum permeability, $\omega = 2\pi f$ is the measurement angular frequency, and $\sigma(\omega) = ne^2\tau/m^*(1 - i\omega)$ is the ac conductivity (here e is the elementary charge, n is the carrier density, m^* is the effective mass of charge carriers, and τ is the relaxation time). Note that θ denotes the Hall angle ($\tan \theta = \sigma_{xy}/\sigma_{xx}$). From Eqs. (6a) and (6b), θ can be related to the ratio of Z_H to Z_L by the following expression:

$$\tan \theta = \frac{Z_H}{Z_L}. \quad (7)$$

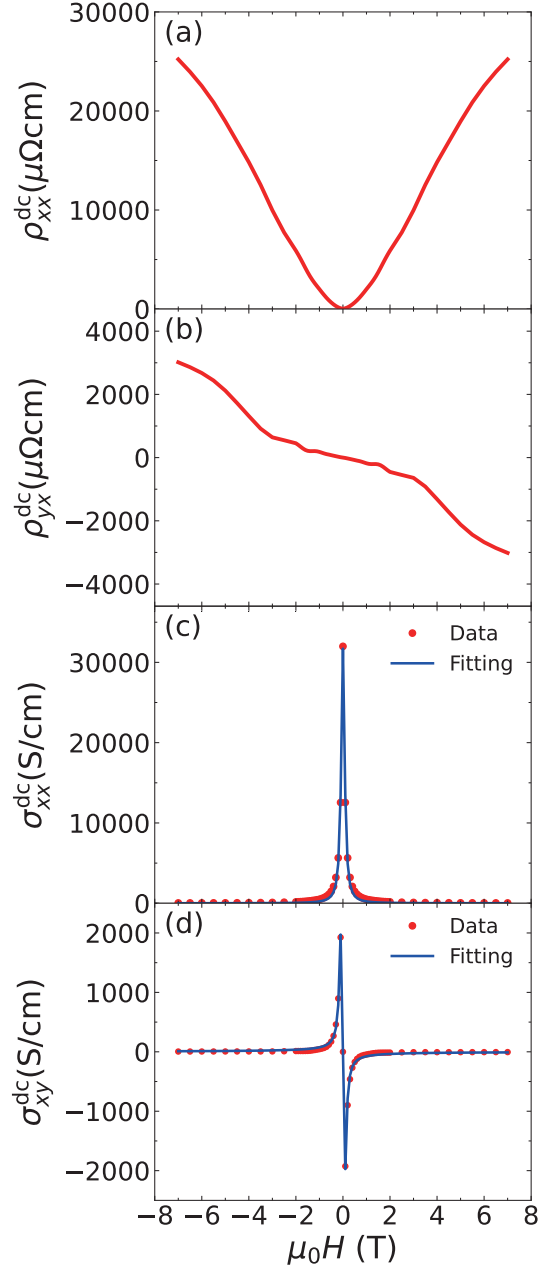


FIG. 3: [(a) and (b)] Magnetic field dependence of the longitudinal resistivity ρ_{xx} (a) and the Hall resistivity ρ_{yx} (b). [(c) and (d)] Magnetic field dependence of the longitudinal conductivity σ_{xx} (c) and Hall conductivity σ_{xy} (d) extracted from Eqs. (B1) and (B2). The red circles represent the experimental data, and the blue solid lines represent the fitting results.

Therefore, the ac Hall angle can be determined by measuring the surface impedance tensor, providing information on the ac Hall conductivity in the skin depth region.

C. Experimental setup and analysis procedure

Our experimental setup for the measurement of the surface impedance tensor is shown in Fig.2. The rutile cavity

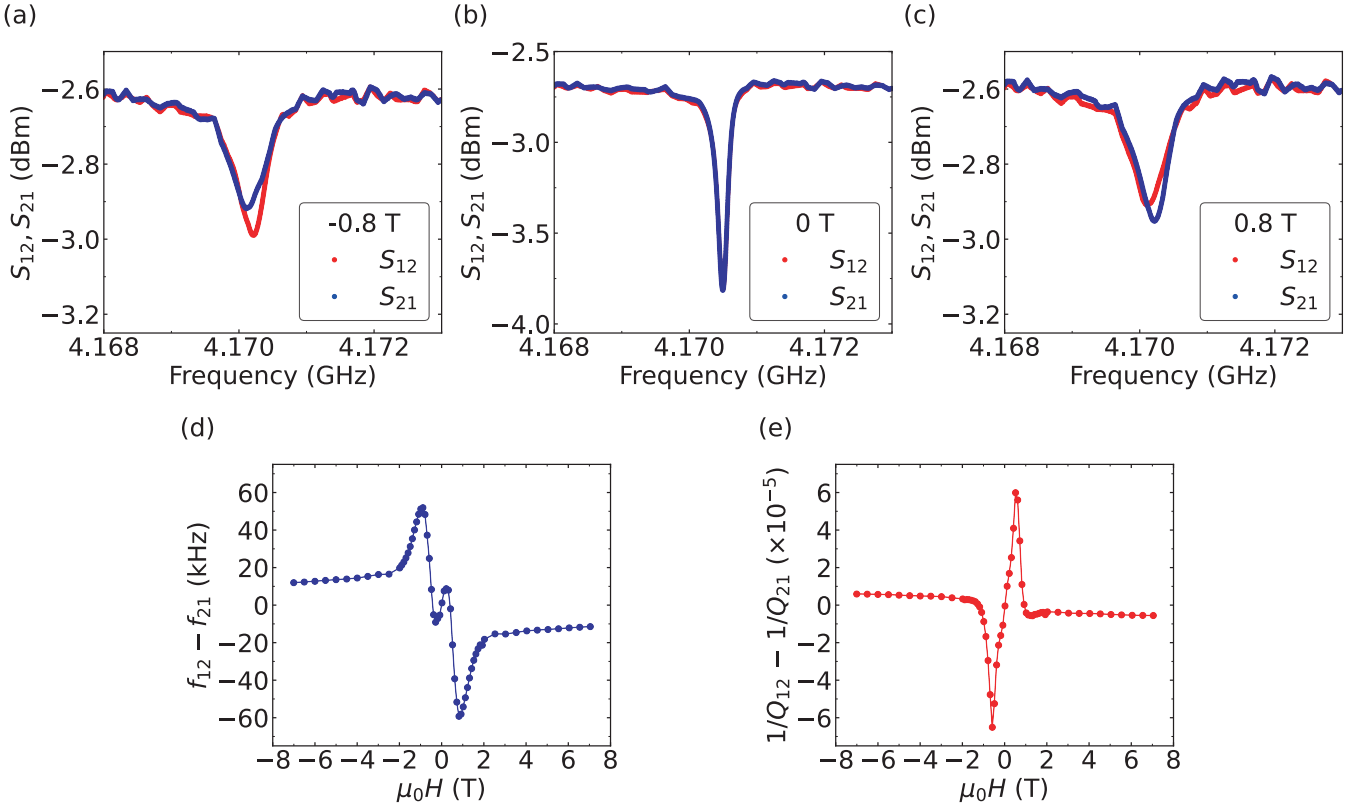


FIG. 4: [(a)-(c)] Resonance spectra of S_{12} (red circles) and S_{21} (blue circles) measured at 10 K for the Bi single crystal at external fields of -0.8 T (a), 0 T (b), and $+0.8$ T (c). [(d) and (e)] Difference in resonant frequency (d) and $1/Q$ (e) between S_{12} and S_{21} at 10 K as a function of magnetic field.

equipped with a hybrid coupler (Orient Microwave, BL32-6347-00), is inserted into a commercial cryostat (Physical Property Measurement System (PPMS), Quantum Design) using a homemade probe. The transmission spectrum of S_{12} and S_{21} is measured by a vector network analyzer (Keysight P5027A) in the room temperature part through semi-rigid coaxial cables. The cylindrical rutile TiO_2 grown by the Verneuil method (Crystal Base Co., Ltd.) is positioned at the center of the copper enclosure with polytetrafluoroethylene (PTFE) spacers. A single crystal of Bi ($320 \mu\text{m}$ (binary) $\times 290 \mu\text{m}$ (bisectrix) $\times 65 \mu\text{m}$ (trigonal)) synthesized by the Czochralski method⁴⁸ is placed at the center of the cylindrical rutile. A sample pack of PPMS was attached to the bottom of the cavity for thermal contact. External dc magnetic fields ($-7 \text{ T} \leq \mu_0 H \leq 7 \text{ T}$) were applied perpendicular to the sample surface (parallel to the trigonal axis) of the Bi single crystal. Our analysis procedure in the surface impedance tensor measurements is as follows:

(1) Determination of R_L and X_L : In Eq. (6a), when the Hagen-Rubens limit $\omega\tau \ll 1$ is satisfied, Z_L can be replaced by

$$Z_L = (1+i) \sqrt{\frac{\mu_0 \omega \rho_{xx}^{\text{dc}}}{2}} \frac{1}{\sqrt{1 \mp i \tan \theta}}, \quad (8)$$

where ρ_{xx}^{dc} is the dc longitudinal resistivity. From this equation, the real and imaginary parts R_L and X_L are given by

$$R_L = \text{Re} \left[(1+i) \sqrt{\frac{\mu_0 \omega \rho_{xx}^{\text{dc}}}{2}} \frac{1}{\sqrt{1 \mp i \tan \theta}} \right], \quad (9a)$$

$$X_L = \text{Im} \left[(1+i) \sqrt{\frac{\mu_0 \omega \rho_{xx}^{\text{dc}}}{2}} \frac{1}{\sqrt{1 \mp i \tan \theta}} \right]. \quad (9b)$$

As shown in the next section, since $\omega\tau \ll 1$ is well satisfied in our Bi single crystal, we can obtain R_L and X_L from Eqs. (9a) and (9b). Here, the correct value of $\tan \theta$ is unknown in step (1) since $\tan \theta$ is a quantity to be finally determined. Therefore, in step (1), we substitute a certain value θ_0 for the Hall angle with reference to the Hall angle obtained from the dc measurements. Then, using R_L and X_L obtained in step (1), $\tan \theta$ is determined through steps (2) and (3). If the value of $\tan \theta$ obtained in step (3) coincides with $\tan \theta_0$ in step (1), the Hall angle can be obtained self-consistently.

(2) Determination of G , C , R_H , and X_H : First, we measure the S_{12} and S_{21} spectra corresponding to the right- and left-handed modes as a function of magnetic field by switching the input and output ports of the circular polarization rutile cavity, from which we obtain $f_{\pm}(H)$ and $Q_{\pm}(H)$. Then, we calculate G and C by comparing Eqs. (4a) and (4b) with Eqs. (9a) and (9b). After that, we extract R_H and X_H from Eqs. (4c) and (4d) by using G .

(3) Calculation of $\tan \theta$: Using each component of the obtained surface impedance tensor, we calculate the ac Hall an-

gle using the following equation:

$$|\tan \theta| = \frac{|Z_H|}{|Z_L|} = \frac{\sqrt{R_H^2 + X_H^2}}{\sqrt{R_L^2 + X_L^2}}. \quad (10)$$

Finally, to confirm the validity of the present measurements and analysis, we compare the results of $\tan \theta$ obtained from Eq. (10) with those obtained from the dc transport measurements. The sign of $\tan \theta$ in Eq. (10) was determined based on the results of $\tan \theta$ from the dc measurements (see Appendix B for details).

III. EXPERIMENTAL RESULTS

A. DC resistivity measurements

As shown in Secs. II B and II C, since the dc resistivity is necessary to obtain the surface impedance tensor, we performed dc resistivity measurements on a Bi single crystal. In this section, we present the results of the dc resistivity measurements (see Appendix B for more details). Figures 3(a) and (b) show the magnetic field dependence of dc longitudinal resistivity (ρ_{xx}^{dc}) and Hall resistivity (ρ_{yx}^{dc}) in our Bi single crystal at 10 K, respectively, where the x and y directions correspond to the binary and bisectrix axes. ρ_{xx}^{dc} shows a giant magnetoresistance due to the high mobility and carrier compensation in Bi (Fig. 3(a)), as reported in previous works⁵². We have also observed a large ρ_{yx}^{dc} in high magnetic fields (Fig. 3(b)), reflecting the lower carrier density compared to other conventional metals. We extracted the longitudinal and transverse (Hall) conductivity σ_{xx}^{dc} and σ_{xy}^{dc} from ρ_{xx}^{dc} and ρ_{yx}^{dc} and analyzed them by simultaneously fitting with the multi-band model (see Appendix C for more details). As a result, we obtained the electron (hole) carrier density $n_{e(h)} = 8.7 \times 10^{17} (8.3 \times 10^{17}) \text{ cm}^{-3}$ and the mobility $\mu_{e(h)} = 1.2 \times 10^5 (9.2 \times 10^4) \text{ cm}^2 \text{ V}^{-1} \text{ s}^{-1}$, respectively. These results are consistent with the previous studies⁴⁹. From $\mu_{e(h)} = e\tau/m^*$ with $m^* = 0.051m_0$ ⁵⁰, we obtained $\tau = 3.4(2.7) \times 10^{-12} \text{ s}$. In the present cavity measurements, $\omega = 2\pi f \sim 2.6 \times 10^{10} \text{ Hz}$, and thus the Hagen-Rubens limit $\omega\tau \ll 1$ is satisfied in our Bi single crystal.

B. Surface impedance tensor measurements

This section presents the results of surface impedance tensor measurements using our circularly polarized rutile cavity. Figures 4(a)-(c) show the resonance spectra of S -parameters for two polarization modes S_{12} and S_{21} measured at -0.8 T , 0 T , and $+0.8 \text{ T}$ at 10 K for the Bi single crystal, respectively. At zero magnetic field, S_{12} and S_{21} show no splitting (Fig. 4(b)). In sharp contrast, S_{12} and S_{21} show clear splitting in the finite external magnetic fields (Figs. 4(a) and (c)). Figures 4(d) and (e) show the difference in the resonance frequency, $f_{12} - f_{21}$, and the energy loss, $1/Q_{12} - 1/Q_{21}$, between the right- and left-handed modes obtained from the fitting of the S_{12} and S_{21} spectra for each magnetic field, where the indices of 12 and 21 correspond to the right (+)- and left (-)-handed modes. We observed distinct field-induced differences between the

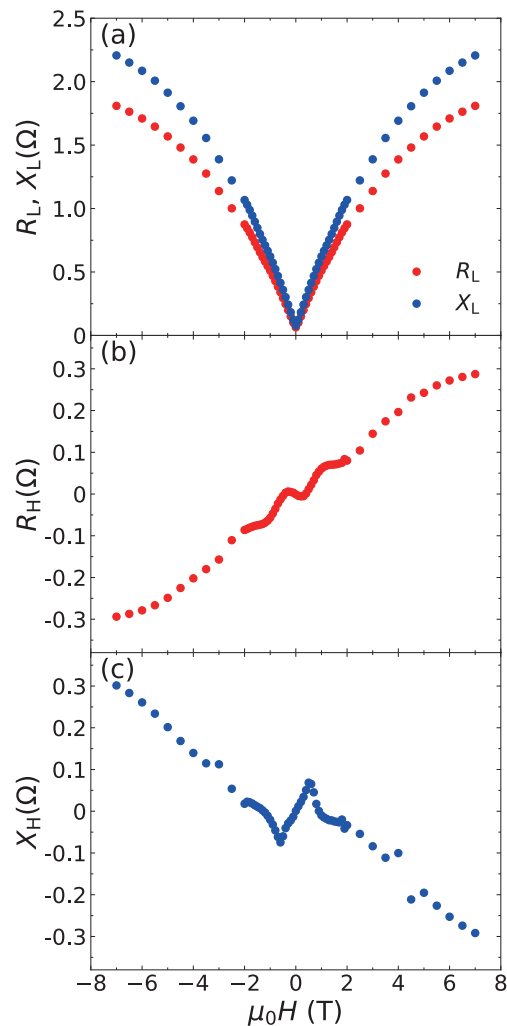


FIG. 5: Magnetic field dependence of each component of the surface impedance tensor measured at 10 K. [(a)-(c)] The real part R_L and imaginary part X_L of the diagonal components (a), and the real part R_H (b) and the imaginary part X_H (c) of the off-diagonal components are shown.

right- and left-handed modes, which are symmetric with respect to the spectrum at zero field. Following the procedure described in Sec. II C, we obtained each component of the surface impedance tensor from the obtained f_{12} , f_{21} , Q_{12} , and Q_{21} , as shown in Figs. 4(d) and (e).

First, we show the magnetic field dependence of R_L and X_L estimated from Eqs. (9a) and (9b) in Fig. 5(a). R_L and X_L show large magnetic field dependence, reflecting the large magnetoresistance of Bi. Next, we derive R_H and X_H as a function of magnetic field, as shown in Figs. 5(b) and (c), respectively, which are obtained from Eqs. (4c) and (4d). Finally, we obtain the Hall angle for each magnetic field from Eq. (10) as shown in Fig. 6. The field dependence of $\tan \theta$ obtained from the circularly polarized rutile cavity is in good agreement with the dc results. Here, we emphasize that $\tan \theta$ obtained from the cavity measurements is the ac Hall angle in the microwave region, and it is expressed $\tan \theta = \omega_c \tau / (1 - i\omega\tau)$ in the Drude model, where $\omega_c = eB/m^*$ is the cyclotron angular frequency (here B is the magnetic flux density). As described in the pre-

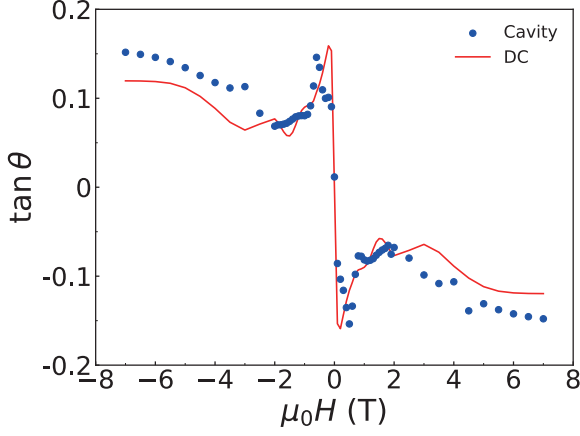


FIG. 6: Magnetic field dependence of $\tan \theta$ obtained from the microwave cavity measurements (blue circles) and dc transport measurements (red solid line) at 10 K.

vious section, since our Bi single crystal satisfies the condition $\omega\tau \ll 1$, the finite frequency correction term $1/(1 - i\omega\tau)$ can be negligible, resulting in the coincidence of the dc and ac Hall angles. This result confirms the validity of our developed method.

IV. SUMMARY

In conclusion, we have developed a circularly polarized microwave cavity with rutile TiO_2 that can maintain a high Q -factor even in magnetic fields and constructed a method to measure the surface impedance tensor. From measurements of tiny Bi single crystals, we have demonstrated that all components of the surface impedance tensor can be accessed from the response of the circularly polarized magnetic field modes. The advantages of the developed method are as follows: (1) Utilizing the cavity perturbation technique, it enables highly sensitive measurements on tiny single crystals in the microwave frequency range. (2) This non-contact method is particularly useful for samples and systems that are difficult to measure by the usual contact method. (3) The experimental setup is straightforward, allowing easy switching between the right- and left-handed circular polarization at cryogenic temperatures.

These advantages can allow precise measurements of the Hall effect in the microwave region, which are particularly useful for systems such as superconductors, where the dc Hall resistance, as well as the dc resistance, becomes zero. The Hall effect measurements in superconductors in the high-frequency regime have the potential to probe TRSB in the superconducting state^{12,13}. Therefore, our newly developed technique provides new insights into Hall measurements in the finite frequency range, offering crucial understanding of exotic phenomena associated with TRSB states in condensed matter physics.

ACKNOWLEDGMENTS

We thank M. Kondo, A. Yamada, K. Kato, and Y. Onishi for fruitful discussions, and Y. Uwatoko for technical support, and N. Miura for sample preparation. This work was supported by CREST (JPMJCR19T5) from Japan Science and Technology (JST), Grants-in-Aid for Scientific Research (KAKENHI) (Nos. JP23H00089, JP23H04862, JP22J21896, JP22H00105, JP22K18681, JP22K18683, JP22K20349, JP22H01964, JP22H01936, JP22K03522, JP21H01793, and JP18KK0375), Grant-in-Aid for Scientific Research on Innovative Areas “Quantum Liquid Crystals” (No. JP19H05824), Transformative Research Areas (A) “Condensed Conjugation” (No. JP20H05869), and the Graduate School of Frontier Sciences, The University of Tokyo, through the Challenging New Area Doctoral Research Grant (Project No. C2316).

Appendix A: Derivation of the principle for the surface impedance tensor measurements

In this APPENDIX section, we derive Eq. (2) in the main text, which connects the surface impedance tensor to the characteristics of the circularly polarized cavity modes.

1. Cavity perturbation method

We overview the conventional cavity perturbation method and derive the ordinary relationship between the resonant properties and the surface impedance of a conductive material. The discussion in this section is based on Refs.^{35,51}.

First, we expand the electromagnetic field eigenmodes, \mathbf{E} and \mathbf{H} , and the current density \mathbf{j} by the solenoidal vectors, \mathbf{e}_a and \mathbf{h}_a , and the irrotational vectors, \mathbf{f}_a and \mathbf{g}_a , where the divergences of \mathbf{e}_a and \mathbf{h}_a are zero ($\nabla \cdot \mathbf{e}_a(\mathbf{h}_a) = 0$) and the rotations of \mathbf{f}_a and \mathbf{g}_a are zero ($\nabla \times \mathbf{f}_a(\mathbf{g}_a) = 0$), as follows:

$$\mathbf{E} = \sum_a \left[\mathbf{e}_a \int_V dV \mathbf{E} \cdot \mathbf{e}_a + \mathbf{f}_a \int_V dV \mathbf{E} \cdot \mathbf{f}_a \right], \quad (\text{A1})$$

$$\mathbf{H} = \sum_a \left[\mathbf{h}_a \int_V dV \mathbf{H} \cdot \mathbf{h}_a + \mathbf{g}_a \int_V dV \mathbf{H} \cdot \mathbf{g}_a \right], \quad (\text{A2})$$

$$\mathbf{j} = \sum_a \left[\mathbf{e}_a \int_V dV \mathbf{j} \cdot \mathbf{e}_a + \mathbf{f}_a \int_V dV \mathbf{j} \cdot \mathbf{f}_a \right]. \quad (\text{A3})$$

Here a is the index indicating the mode of interest, which is orthonormalized with respect to each of the other modes. \mathbf{e}_a , \mathbf{h}_a , \mathbf{f}_a , and \mathbf{g}_a satisfy the following relation and boundary conditions at the surface of a sample and a cavity,

$$k_a \mathbf{e}_a = \nabla \times \mathbf{h}_a, \quad k_a \mathbf{h}_a = \nabla \times \mathbf{e}_a, \quad (\text{A4})$$

$$k_a \mathbf{f}_a = \nabla \psi_a, \quad k_a \mathbf{g}_a = \nabla \phi_a, \quad (\text{A5})$$

$$\mathbf{n} \times \mathbf{e}_a = 0, \quad \mathbf{n} \cdot \mathbf{h}_a = 0, \quad \psi_a = 0, \quad \phi_a = 0, \quad (\text{A6})$$

$$\mathbf{n} \times \mathbf{h}_a = 0, \quad \mathbf{n} \cdot \mathbf{e}_a = 0, \quad \psi_a = 0, \quad \phi_a = 0, \quad (\text{A7})$$

where k_a is the propagation constant, and ψ_a and ϕ_a are the scalar field for \mathbf{f}_a and \mathbf{g}_a , respectively. Eqs. (A6) and (A7)

are the boundary conditions on a conductive and an insulating surface, respectively, and \mathbf{n} is the unit vector perpendicular to the surface.

Then, we expand Eqs. (A1), (A2), and (A3), and substitute them into Maxwell's equations and extract only a component, from which the following equations can be derived

$$k_a \int_V dV \mathbf{E} \cdot \mathbf{e}_a + \int_{S_c} dS (\mathbf{n} \times \mathbf{E}) \cdot \mathbf{h}_a = -\mu_0 \frac{\partial}{\partial t} \int_V dV \mathbf{H} \cdot \mathbf{h}_a, \quad (\text{A8})$$

$$\begin{aligned} k_a \int_V dV \mathbf{H} \cdot \mathbf{h}_a + \int_{S_i} dS (\mathbf{n} \times \mathbf{H}) \cdot \mathbf{e}_a \\ = \varepsilon_0 \frac{\partial}{\partial t} \int_V dV \mathbf{E} \cdot \mathbf{e}_a - \int_V dV \mathbf{j} \cdot \mathbf{e}_a, \end{aligned} \quad (\text{A9})$$

where S_c is the conducting surface, S_i is the insulating surface, and V is the volume of the cavity. We arranged these equations as follows:

$$\begin{aligned} (k_a^2 + \varepsilon_0 \mu_0 \frac{\partial^2}{\partial t^2}) \int_V dV \mathbf{E} \cdot \mathbf{e}_a \\ = -k_a \int_{S_c} dS (\mathbf{n} \times \mathbf{E}) \cdot \mathbf{h}_a \\ + \mu_0 \frac{\partial}{\partial t} \int_{S_i} dS (\mathbf{n} \times \mathbf{H}) \cdot \mathbf{e}_a - \mu_0 \frac{\partial}{\partial t} \int_V dV \mathbf{j} \cdot \mathbf{e}_a, \end{aligned} \quad (\text{A10})$$

$$\begin{aligned} (k_a^2 + \varepsilon_0 \mu_0 \frac{\partial^2}{\partial t^2}) \int_V dV \mathbf{H} \cdot \mathbf{h}_a \\ = -\varepsilon_0 \frac{\partial}{\partial t} \int_{S_c} dS (\mathbf{n} \times \mathbf{E}) \cdot \mathbf{h}_a \\ - k_a \int_{S_i} dS (\mathbf{n} \times \mathbf{H}) \cdot \mathbf{e}_a + k_a \int_V dV \mathbf{j} \cdot \mathbf{e}_a. \end{aligned} \quad (\text{A11})$$

Here, in an ideal cavity surrounded by a perfect conducting surface, the right-hand side of Eq. (A10) is zero. Then, we can obtain the following relation for the dispersion of the electromagnetic field by considering the time revolution of $e^{-i\omega t}$,

$$\omega_a = \frac{1}{\sqrt{\varepsilon_0 \mu_0}} k_a. \quad (\text{A12})$$

From this equation, Eq. (A11) is rewritten by

$$\begin{aligned} i \left(\frac{\omega}{\omega_a} - \frac{\omega_a}{\omega} \right) \int_V dV \mathbf{H} \cdot \mathbf{h}_a = \frac{1}{\omega_a \mu_0} \int_{S_c} dS (\mathbf{n} \times \mathbf{E}) \cdot \mathbf{h}_a \\ + \frac{i}{\omega \sqrt{\varepsilon_0 \mu_0}} \left(\int_{S_i} dS (\mathbf{n} \times \mathbf{H}) \cdot \mathbf{e}_a - \int_V dV \mathbf{j} \cdot \mathbf{e}_a \right). \end{aligned} \quad (\text{A13})$$

An actual cavity has dissipation, and the complex angular resonance frequency $\hat{\omega}$ of the cavity in the mode a can be expressed using the deviation $\delta \hat{\omega}_a$ from the ideal cavity and the Q -factor as follows:

$$\hat{\omega} = \hat{\omega}_a + \delta \hat{\omega}_a \simeq \omega_a - \frac{i\omega_a}{2Q} + \delta \omega_a. \quad (\text{A14})$$

If the dissipation is perturbative ($Q \gg 1$), we can obtain from Eq. (A14)

$$\frac{i}{2} \left(\frac{\omega}{\omega_a} - \frac{\omega_a}{\omega} \right) \simeq \frac{1}{2Q} + i \frac{\delta \omega_a}{\omega_a}. \quad (\text{A15})$$

From Eqs. (A13) and (A15), we can obtain the following relationship:

$$\begin{aligned} \frac{1}{2Q} + i \frac{\delta \omega_a}{\omega_a} \simeq \frac{1}{\omega_a} \left(\frac{\int_{S_c} dS (\mathbf{n} \times \mathbf{E}) \cdot \mathbf{h}_a}{2\mu_0 \int_V dV \mathbf{H} \cdot \mathbf{h}_a} \right. \\ \left. - \frac{i}{2Z_0 \varepsilon_0} \frac{\int_V dV \mathbf{j} \cdot \mathbf{e}_a}{\int_V dV \mathbf{H} \cdot \mathbf{h}_a} + \frac{i}{2Z_0 \varepsilon_0} \frac{\int_{S_i} dS (\mathbf{n} \times \mathbf{H}) \cdot \mathbf{e}_a}{\int_V dV \mathbf{H} \cdot \mathbf{h}_a} \right), \end{aligned} \quad (\text{A16})$$

where $Z_0 = \sqrt{\mu_0/\varepsilon_0}$ represents the vacuum impedance. Here, we consider the perturbation response when a small conducting sample is placed in the antinode of the magnetic field mode in the cavity. The second term on the right-hand side of Eq. (A16) indicates the Joule heating contribution due to the resistance of the sample and the cavity walls. If the sample is sufficiently smaller than the cavity volume, the contribution from the sample is negligible. The third term is the contribution from the insulating surface. Therefore, only the first term contributes to the response of the conducting sample. Then, considering the difference Δ with and without the sample, the second and third terms can be subtracted as background contributions, and we can obtain the following essential relationship between the magnetic field mode and the frequency properties in the cavity perturbation method as follows:

$$\Delta \left(\frac{1}{2Q} + i \frac{\delta \omega_a}{\omega_a} \right) = \Delta \left(\frac{1}{2Q} \right) + i \left(\frac{\Delta \omega}{\omega_a} + C \right) = \frac{\int_S dS (\mathbf{n} \times \mathbf{E}) \cdot \mathbf{h}_a}{2\mu_0 \omega_a \int_V dV \mathbf{H} \cdot \mathbf{h}_a}. \quad (\text{A17})$$

2. Principle of the surface impedance tensor measurements

In this section, we extend Eq. (A17) to the case of circularly polarized magnetic field modes. First, we introduce the degree of freedom for the right (+)- and left (-)-handed polarized modes into Eq. (A17) as follows:

$$\Delta \left(\frac{1}{2Q_{\pm}} \right) + i \left(\frac{\Delta \omega_{\pm}}{\omega_0} + C \right) = \frac{\int_S dS (\mathbf{n} \times \mathbf{E}) \cdot \mathbf{H}_a}{2\omega_0 \mu_0 \int_V \mathbf{H} \cdot \mathbf{H}_a dV}, \quad (\text{A18})$$

where \mathbf{H}_a is the circularly polarized H -field mode we are currently focusing on. Next, we get a specific expression for $\int_S dS (\mathbf{n} \times \mathbf{E}) \cdot \mathbf{H}_a$. Let us consider the basis expansion of the right- and left-handed circularly polarized H -field modes in the xy -plane of TM_{\pm} modes as shown in Sec. II A. They are described as

$$\mathbf{H}_a = h \begin{pmatrix} 1 \\ 0 \end{pmatrix} + h \begin{pmatrix} 0 \\ \pm i \end{pmatrix}, \quad (\text{A19})$$

where h is the amplitude of the H -field mode. We decompose the circularly polarized mode H_a into two linearly polarized basic vectors with a phase difference of $\pm \frac{\pi}{2}$ as follows:

$$\mathbf{H}_A = h \begin{pmatrix} 1 \\ 0 \end{pmatrix}, \quad (\text{A20a})$$

$$\mathbf{H}_B = h \begin{pmatrix} 0 \\ \pm i \end{pmatrix}. \quad (\text{A20b})$$

Then, \mathbf{H}_a can be expressed as

$$\begin{aligned} \mathbf{H}_a \approx \mathbf{H}_A \int_V \mathbf{H} \cdot \mathbf{H}_A dV + \mathbf{H}_B \int_V \mathbf{H} \cdot \mathbf{H}_B dV \\ = h \left(\int_V \mathbf{H} \cdot \mathbf{H}_A dV \right) \begin{pmatrix} 1 \\ 0 \end{pmatrix} + h \left(\int_V \mathbf{H} \cdot \mathbf{H}_B dV \right) \begin{pmatrix} 0 \\ \pm i \end{pmatrix}. \end{aligned} \quad (\text{A21})$$

Next, we consider the specific form of $(\mathbf{n} \times \mathbf{E}) \cdot \mathbf{H}_a$. In this case, the ratio of the E and H -field components parallel to the sample surface is defined by the surface impedance tensor Eq. (1) as

$$\begin{aligned} \mathbf{n} \times \mathbf{E} &= \tilde{\mathbf{Z}}\mathbf{H} \\ &= \tilde{\mathbf{Z}}\mathbf{H}_a \\ &= h \begin{pmatrix} Z_L \int_V \mathbf{H} \cdot \mathbf{H}_A dV \pm iZ_H \int_V \mathbf{H} \cdot \mathbf{H}_B dV \\ -Z_H \int_V \mathbf{H} \cdot \mathbf{H}_A dV \pm iZ_L \int_V \mathbf{H} \cdot \mathbf{H}_B dV \end{pmatrix}. \end{aligned} \quad (\text{A22})$$

Here, we consider that the component of the total magnetic field H parallel to the sample surface (xy -plane), which contributes to the surface impedance, is \mathbf{H}_a . From Eqs. (A21) and (A22), $(\mathbf{n} \times \mathbf{E}) \cdot \mathbf{H}_a$ is expressed as

$$\begin{aligned} (\mathbf{n} \times \mathbf{E}) \cdot \mathbf{H}_a &= h^2 [Z_L \left(\int_V \mathbf{H} \cdot \mathbf{H}_A dV - \int_V \mathbf{H} \cdot \mathbf{H}_B dV \right) \\ &\quad \mp iZ_H \left(\int_V \mathbf{H} \cdot \mathbf{H}_A dV - \int_V \mathbf{H} \cdot \mathbf{H}_B dV \right)]. \end{aligned} \quad (\text{A23})$$

The substitution of Eq. (A23) into Eq. (A18) leads to the following relationship between the resonant properties (frequency and Q -factor) and the surface impedance tensor

$$\begin{aligned} \Delta \left(\frac{1}{2Q_{\pm}} \right) + i \left(\frac{\Delta\omega_{\pm}}{\omega_0} + C \right) &= \frac{\int_S h^2 ds}{2\omega_0\mu_0 \int_V \mathbf{H} \cdot \mathbf{H}_A dV} \\ &\quad \times \left\{ Z_L \left(\int_V \mathbf{H} \cdot \mathbf{H}_A dV - \int_V \mathbf{H} \cdot \mathbf{H}_B dV \right) \right. \\ &\quad \left. \mp iZ_H \left(\int_V \mathbf{H} \cdot \mathbf{H}_A dV - \int_V \mathbf{H} \cdot \mathbf{H}_B dV \right) \right\} \\ &= G(Z_L \mp iZ_H), \end{aligned} \quad (\text{A24})$$

where ω_0 is the resonance frequency without the sample, and the geometric factor G is defined by

$$G = \frac{\int_S h^2 ds}{2\omega_0\mu_0 \int_V \mathbf{H} \cdot \mathbf{H}_A dV} \left(\int_V \mathbf{H} \cdot \mathbf{H}_A dV - \int_V \mathbf{H} \cdot \mathbf{H}_B dV \right). \quad (\text{A25})$$

As a result, we derive Eq. (2) in the main text, which connects the surface impedance tensor to the characteristics of the circularly polarized cavity modes.

Appendix B: Details of dc transport measurements

Our dc transport measurements were performed by the 5-terminal method using PPMS. We obtained ρ_{xx} and ρ_{yx} , and calculated σ_{xx} and σ_{xy} by using the following relations:

$$\sigma_{xx} = \frac{\rho_{xx}}{\rho_{xx}^2 + \rho_{yx}^2}, \quad (\text{B1})$$

$$\sigma_{xy} = \frac{\rho_{yx}}{\rho_{xx}^2 + \rho_{yx}^2}. \quad (\text{B2})$$

To investigate the validity of our measurements and the quality of our Bi sample, we fitted σ_{xx} and σ_{xy} with the following equations in the two-carrier model.

$$\sigma_{xx} = \frac{n_e e \mu_e}{1 + (\mu_e B)^2} + \frac{n_h e \mu_h}{1 + (\mu_h B)^2}, \quad (\text{B3})$$

$$\sigma_{xy} = -\frac{n_e e \mu_e^2 B}{1 + (\mu_e B)^2} + \frac{n_h e \mu_h^2 B}{1 + (\mu_h B)^2}, \quad (\text{B4})$$

where n is the carrier density, μ is the mobility, and the subscripts e and h are indexes for electron and hole carriers, respectively.

AUTHOR DECLARATIONS

Data Availability Statement

The data that support the findings of this study are available from the corresponding authors upon reasonable request.

Conflict of Interest

The authors have no conflicts to disclose.

REFERENCES

- ¹E. H. Hall, American Journal of Mathematics **2**, 287 (1879).
- ²N. Nagaosa, J. Sinova, S. Onoda, A. H. MacDonald, and N. P. Ong, Rev. Mod. Phys. **82**, 1539 (2010).
- ³D. M. Mittleman, J. Cunningham, M. C. Nuss, and M. Geva, Applied Physics Letters **71**, 16 (1997).
- ⁴R. Shimano, Y. Ino, Y. P. Svirko, and M. Kuwata-Gonokami, Applied Physics Letters **81**, 199 (2002).
- ⁵Y. Ikebe and R. Shimano, Applied Physics Letters **92**, 012111 (2008).
- ⁶Y. Ikebe, T. Morimoto, R. Masutomi, T. Okamoto, H. Aoki, and R. Shimano, Phys. Rev. Lett. **104**, 256802 (2010).
- ⁷R. Shimano, Y. Ikebe, K. S. Takahashi, M. Kawasaki, N. Nagaosa, and Y. Tokura, Europhysics Letters **95**, 17002 (2011).
- ⁸R. Shimano, G. Yumoto, J. Yoo, R. Matsunaga, S. Tanabe, H. Hibino, T. Morimoto, and H. Aoki, Nature Communications **4**, 1841 (2013).
- ⁹K. N. Okada, Y. Takahashi, M. Mogi, R. Yoshimi, A. Tsukazaki, K. S. Takahashi, N. Ogawa, M. Kawasaki, and Y. Tokura, Nature Communications **7**, 12245 (2016).
- ¹⁰Y. Okamura, S. Minami, Y. Kato, Y. Fujishiro, Y. Kaneko, J. Ikeda, J. Muramoto, R. Kaneko, K. Ueda, V. Kocsis, *et al.*, Nature Communications **11**, 4619 (2020).
- ¹¹T. Matsuda, N. Kanda, T. Higo, N. Armitage, S. Nakatsuji, and R. Matsunaga, Nature Communications **11**, 909 (2020).
- ¹²J. Xia, Y. Maeno, P. T. Beyersdorf, M. M. Fejer, and A. Kapitulnik, Phys. Rev. Lett. **97**, 167002 (2006).
- ¹³E. R. Schemm, W. J. Gannon, C. M. Wishne, W. P. Halperin, and A. Kapitulnik, Science **345**, 190 (2014).
- ¹⁴S. P. Cooke, Phys. Rev. **74**, 701 (1948).
- ¹⁵A. M. Portis and D. Teaney, Journal of Applied Physics **29**, 1692 (1958).
- ¹⁶G. Hambleton and W. Gärtner, Journal of Physics and Chemistry of Solids **8**, 329 (1959).
- ¹⁷N. Watanabe, Journal of the Physical Society of Japan **16**, 1979 (1961).
- ¹⁸Y. Nishina and G. C. Danielson, Review of Scientific Instruments **32**, 790 (1961).
- ¹⁹R. Pethig, Journal of Biological Physics **1**, 193 (1973).
- ²⁰M. M. Sayed and C. R. Westgate, Review of Scientific Instruments **46**, 1074 (1975).
- ²¹M. M. Sayed and C. R. Westgate, Review of Scientific Instruments **46**, 1080 (1975).
- ²²J. R. Fletcher, Journal of Physics E: Scientific Instruments **9**, 481 (1976).
- ²³N. P. Ong and A. M. Portis, Phys. Rev. B **15**, 1782 (1977).
- ²⁴T. E. Cross and R. Pethig, International Journal of Quantum Chemistry **18**, 385 (1980).
- ²⁵N. P. Ong, W. Bauhofer, and C. Wei, Review of Scientific Instruments **52**, 1367 (1981).
- ²⁶D. Eley and N. C. Lockhart, Journal of Physics E: Scientific Instruments **16**, 47 (1983).
- ²⁷F. Kuchar, R. Meisels, G. Weimann, and W. Schlapp, Phys. Rev. B **33**, 2965 (1986).

- ²⁸M. Dressel, H. Helberg, and D. Schweitzer, *Synthetic Metals* **42**, 2043 (1991), proceedings of the International Conference on Science and Technology of Synthetic Metals.
- ²⁹B.-K. Na, M. A. Vannice, and A. B. Walters, *Phys. Rev. B* **46**, 12266 (1992).
- ³⁰L. Chen, C. Ong, and B. Tan, *IEEE Transactions on Magnetics* **34**, 272 (1998).
- ³¹E. Prati, S. Faralli, M. Martinelli, G. Annino, G. Biasiol, and L. Sorba, *Review of Scientific Instruments* **74**, 154 (2003).
- ³²A. Y. Al-Zoubi and O. M. Hasan, *Journal of Physics: Conference Series* **13**, 430 (2005).
- ³³D. V. B. Murthy, V. Subramanian, and V. R. K. Murthy, *Review of Scientific Instruments* **77**, 066108 (2006).
- ³⁴D. V. B. Murthy, V. Subramanian, B. Sundaray, and T. S. Natarajan, *Applied Physics Letters* **92**, 222111 (2008).
- ³⁵R. Ogawa, T. Okada, H. Takahashi, F. Nabeshima, and A. Maeda, *Journal of Applied Physics* **129**, 015102 (2021).
- ³⁶R. Ogawa, F. Nabeshima, T. Nishizaki, and A. Maeda, *Phys. Rev. B* **104**, L020503 (2021).
- ³⁷R. Ogawa, F. Nabeshima, and A. Maeda, *Journal of the Physical Society of Japan* **92**, 064707 (2023).
- ³⁸T. Arakawa, T. Oka, S. Kon, and Y. Niimi, *Phys. Rev. Lett.* **129**, 046801 (2022).
- ³⁹T. Arakawa, S. Norimoto, S. Iwakiri, T. Asano, and Y. Niimi, *Review of Scientific Instruments* **90**, 084707 (2019).
- ⁴⁰H. Kitano, R. Matsuo, K. Miwa, A. Maeda, T. Takenobu, Y. Iwasa, and T. Mitani, *Phys. Rev. Lett.* **88**, 096401 (2002).
- ⁴¹J. Golm, S. Arguedas Cuendis, S. Calatroni, C. Cogollos, B. Döbrich, J. Gallego, J. García Barceló, X. Granados, J. Gutierrez, I. Irastorza, T. Koettig, N. Lamas, J. Liberadzka-Porret, C. Malbrunot, W. Millar, P. Navarro, C. Carlos, T. Puig, G. Rosaz, M. Siodlaczek, G. Telles, and W. Wuensch, *IEEE Transactions on Applied Superconductivity* **32**, 1 (2022).
- ⁴²S. Posen, M. Checchin, O. Melnychuk, T. Ring, I. Gonin, and T. Khabiboulline, *Phys. Rev. Appl.* **20**, 034004 (2023).
- ⁴³W. Huttema, B. Morgan, P. Turner, W. Hardy, X. Zhou, D. Bonn, R. Liang, and D. Broun, *Review of Scientific Instruments* **77** (2006).
- ⁴⁴S. Donovan, O. Klein, M. Dressel, K. Holczer, and G. Grüner, *International Journal of Infrared and Millimeter Waves* **14**, 2459 (1993).
- ⁴⁵T. Shibauchi, H. Kitano, K. Uchinokura, A. Maeda, T. Kimura, and K. Kishio, *Phys. Rev. Lett.* **72**, 2263 (1994).
- ⁴⁶K. Hashimoto, T. Shibauchi, S. Kasahara, K. Ikada, S. Tonegawa, T. Kato, R. Okazaki, C. J. van der Beek, M. Konczykowski, H. Takeya, K. Hirata, T. Terashima, and Y. Matsuda, *Phys. Rev. Lett.* **102**, 207001 (2009).
- ⁴⁷K. Hashimoto, K. Cho, T. Shibauchi, S. Kasahara, Y. Mizukami, R. Katsumata, Y. Tsuruhara, T. Terashima, H. Ikeda, M. A. Tanatar, H. Kitano, N. Salovich, R. W. Giannetta, P. Walmsley, A. Carrington, R. Prozorov, and Y. Matsuda, *Science* **336**, 1554 (2012).
- ⁴⁸K. Hiruma, G. Kido, and N. Miura, *Journal of the Physical Society of Japan* **51**, 3278 (1982).
- ⁴⁹J. P. Michenaud and J. P. Issi, *Journal of Physics C: Solid State Physics* **5**, 3061 (1972).
- ⁵⁰G. E. Everett, *Phys. Rev.* **128**, 2564 (1962).
- ⁵¹J. C. Slater, *Rev. Mod. Phys.* **18**, 441 (1946).
- ⁵²B. Fauqué, B. Vignolle, C. Proust, J.-P. Issi, and K. Behnia, *New Journal of Physics* **11**, 113012 (2009).